HHS Public Access
Author manuscript
IEEE Trans Med Imaging. Author manuscript; available in PMC 2020 February 01.

Published in final edited form as:
IEEE Trans Med Imaging. 2019 February ; 38(2): 337–348. doi:10.1109/TMI.2018.2864944.

An Empirical Data Inconsistency Metric (DIM) Driven CT Image Reconstruction Method

Yinsheng Li[1], **Guang-Hong Chen**[1,2]

[1.]Department of Medical Physics at the University of Wisconsin-Madison.

[2.]Department of Radiology at the University of Wisconsin-Madison.

Abstract

Current CT image reconstruction methods generally assume that a complete and consistent data set was acquired during data acquisition. In practice, however, the acquired data are often not consistent from one view angle to another. In this case, the application of a well developed image reconstruction algorithm to an inconsistent data set still generates artifacts in the reconstructed images. Therefore, it is highly desirable to develop a simple method to classify the acquired data set into several consistency classes and to incorporate the data consistency information into an image reconstruction framework to simultaneously reconstruct several sub-images of the same image object according to the data consistency level of the acquired data set. In this work, an empirical data inconsistency metric (DIM) was introduced to characterize the inconsistency level of the acquired cone beam CT projection data at each view angle caused by the polychromatic x-ray spectrum and the use of tube potential modulation. The entire acquired data set is then sorted into several subsets of view angles based upon the value of the DIM at each view angle. After data classification, the previously published algorithm, synchronized multiartifact reduction with tomographic reconstruction (SMART-RECON), was applied to simultaneously reconstruct images for these sub-images in different spectral consistency classes. Each sub-image is consistent with the subset of the projection view angles for a given range of DIM values. To validate the method, numerical simulation studies from an anthropomorphic numerical phantom, a hybrid phantom of known truth with human anatomy, and *in vivo* human subject data were conducted to demonstrate the practical utility of the proposed method.

Keywords

Computed Tomography; Data Consistency; Statistical Image Reconstruction; SMART-RECON; Spectral-inconsistency

I. Introduction

IN the past decade or so, tremendous progress has been made in computed tomography (CT) image reconstruction. Breakthroughs include the development of mathematically exact analytical image reconstruction methods [1] that nicely handle the so-called long object

Scientific correspondence should be addressed to Guang-Hong Chen: gchen7@wisc.edu.

problem [2], [3], [4], [5], [6], and the targeted region-of-interest (ROI) reconstruction problem from incomplete data sets [7], [8], [9], [4], [5], [6]. In recent years, primarily motivated by the attempt to reduce radiation dose [10], iterative reconstruction methods have been intensively investigated [11]. Some iterative reconstruction algorithms focus on addressing the image reconstruction problems for vastly undersampled data sets [12], [13] while some other algorithms focus on improving temporal resolution [14], [15].

In practice, an elegant reconstruction method having all the requisite scientific rigor does not necessarily warrant an artifact-free reconstruction due to the presence of noise, motion, contrast variation and other non-ideal physical factors in the acquired projection data set. As a matter of fact, when a reconstruction algorithm is developed, it is often assumed that a sufficient and consistent projection data set is available for use. When the data sufficiency condition and/or data consistency condition are/is violated, image artifacts are inevitably present in the reconstructed image. Note that data sufficiency conditions are more clearly defined for analytical image reconstruction [16], yet remain unclear for iterative reconstruction methods despite the progress in compressive/compressed sensing theory [17], [18]. Therefore, to facilitate the discussion of data consistency conditions which are relevant to this work, we assumed that the acquired data is sufficient for conventional image reconstruction methods.

In discussions of image reconstruction, we often assume that the image object remains stationary during data acquisitions and the acquired data can be perfectly linearized by the logarithmic operation to obtain the line integral data of the attenuation coefficients. However, these assumptions are often violated in practice, such as in dynamic CT acquisitions in which either the image object moves (e.g., cardiac CT) or the attenuation coefficients of the image object evolve with time (e.g., contrast enhanced CT exam). The use of polychromatic x-ray spectra in data acquisitions introduces nonlinearity and thus the log-process does not yield the desired line integral data. The situation can be further exacerbated by the fact that the hetereogeneity and anisotropy of the image object make the beam hardening effects depend on both the image object content and x-ray beam directions. In some data acquisitions, due to the limited dynamic range of the used digital detector in data acquisition, the so-called auto-exposure-control (AEC) is often used to modulate the tube current and/or tube potential such that the available detector dynamic range is fully utilized to generate image contrast. In all these real life cases, the acquired data would be intrinsically inconsistent from one view angle to another. Direct use of image reconstruction methods, which do not take data inconsistency into account, would yield images with artifacts. Therefore, a good understanding of the consistency level of the acquired projection data set may shed new light on the root cause of image artifacts and potential methods to correct the image artifacts.

Significant progress has been made in the study of data consistency conditions of an acquired data set. These consistency conditions include the Helgason-Ludwig moment conditions [19], [20], which have been extensively studied for a set of parallel-beam projections and extended to divergent fan-beams using rebinning strategies. Several consistency conditions were developed directly for divergent-beam geometry: the use of John’s equation for cone-beam projections [21], [22]; the extension of John’s equation for straight line source trajectory [23]; the integral invariant condition [24]; the parallel-fan-beam Hilbert projection equality [25] and the associated data consistency condition [26]; and the new range conditions for cone beam projections [27]. These consistency conditions have also been proposed as guiding principles to either complete the missing line integrals or to compensate for the object movement [28]. In a nutshell, these consistency conditions mainly tell us what conditions the projection data set *should satisfy* for specific source trajectories, but they generally do not tell us *to what degree* the data at a given projection view angle *is inconsistent* with the data acquired at the other view angles. In this sense, these data consistency conditions are *global* conditions. At least, they are not sufficiently *local* to characterize the consistency level of the data acquired at one view angle relative to the data acquired at other view angles. Thus it is not easy to incorporate these data consistency conditions into the reconstruction process in order to reduce image artifacts.

As it has been mentioned earlier, there are many different causes that result in data inconsistency in the acquired data. Some causes such as cardiac motion can be very complicated and thus there is no easy way to classify data while other cases can be relatively simple to allow the acquired data be intuitively classified into difference classes [29], [30], [31]. The purpose of this paper was to introduce an empirical data inconsistency metric (DIM) to quantify data inconsistency caused by the use of polychromatic x-rays and the use of tube potential modulation, to classify the acquired projection data into different spectral consistency classes using the defined DIM, and then to incorporate the evaluation of data consistency into a recently developed iterative reconstruction method to simultaneously reconstruct images for each consistency class with reduced image artifacts. As an example, this paper focuses on a specific type of data inconsistency: the spectral inconsistency caused by the use of a polychromatic x-ray spectrum in CT data acquisitions.

II. Methods

The empirical data consistency metric in this paper was motivated by the following simple observations: (1) When an image does not contain image artifacts, a forward projection of the image yields a consistent projection data set. Conversely, when a reconstructed image is contaminated with artifacts, the projection data set used to perform that image reconstruction is then referred to as an inconsistent data set. (2) A simple image segmentation technique can be used to segment an artifact contaminated image into an artifact-free image; this artifact-free image is referred to as a prior image in this work. (3) A forward projection of this artifact-free prior image is used to generate a consistent data set, and this consistent data set is used to assess the degree of data inconsistency level for the original input projection data set at each view angle. The details of the method are presented in the following sub-sections.

A. Empirical data inconsistency metric (DIM) for projection data at a given view angle and the gross DIM (gDIM) for a given angular range

1) Generation of the prior image: The prior image in this paper is generated from the image reconstructed using the filtered backprojection (FBP) method and the short-scan data acquired from the polychromatic x-ray spectrum. An intensity-based image segmentation method was used to generate the prior image. Specifically, the FBP reconstructed image was segmented into three different tissue types using intensity-thresholding values: air, soft tissue, and bone [32]. Typically, for an image corresponding to a noncontrast-enhanced image object, each voxel with intensity values varying from −500 HU to 500 HU are identified as soft tissue and voxels with intensity values beyond 500 HU are identified as bone. Voxels identified as soft tissue are then set to the linear attenuation coefficients of soft-tissues using the database provided by NIST for a selected reference x-ray energy. After image segmentation, the prior image is then forward projected using this selected reference x-ray energy to generate a reference consistent data set. In this paper, the reference energy was selected to be 43 keV, which corresponds to the mean energy of a typical x-ray spectrum generated using a 70 kVp tube potential.

2) Data inconsistency metric (DIM) for the projection data acquired at a given view angle: The data inconsistency metric (DIM) is defined to quantify the level of data inconsistency at each view angle. It is defined as the relative difference between the acquired projection data (i.e., the log-processed data after data corrections such as the bad pixel correction, flood field and dark field correction, gain correction etc.) at a given view angle and the corresponding synthetic projection data generated from a forward projection of the prior image at the same view angle with the selected reference x-ray energy:

$$\mathrm{D}_1(v) = \left\| \mathscr{Y}(v) - \mathscr{Y}_p(v) \right\|_2, \quad (1)$$

where v is the view angle, $\mathscr{Y}(v)$ is the measured projection data at the v-th view angle, and $\mathscr{Y}_p$ is the synthetic forward projection of the prior image.

For the sake of convenience, the DIM is normalized as follows:

$$\mathrm{D}_2(v) = \frac{D_1(v)}{\max\left\{\mathrm{D}_1(v)\right\}}, \quad (2)$$

$$\mathrm{DIM}(v) = \mathrm{D}_2(v) - \min\left\{\mathrm{D}_2(v)\right\} \ \in [0, 1), \quad (3)$$

where $\max\{\mathrm{D}_1(v)\}$ is the maximal value of $\mathrm{D}_1(v)$ while $\min\{\mathrm{D}_2(v)\}$ is the minimal value of $\mathrm{D}_2(v)$. The maximal DIM value of a data set may be equal to or smaller than 1, and the minimal DIM value of a data set is always normalized to 0.

3) Gross DIM (gDIM) for a set of view angles in an angular range: When a data set consists of multiple view angles, an averaged DIM which is referred to as gDIM is defined to quantify the gross data inconsistency level:

$$\mathrm{gDIM}(t) = \frac{1}{N_t} \sum_{v \in C_t} \mathrm{DIM}(v), \quad (4)$$

where C_t is a set of view angles. The normalization factor, N_t, is the number of view angles within the t-th class.

4) DIM-based data sorting scheme: The view angles for a specific consistency class are selected according to the following definition:

$$C_t = \left\{ v \middle| b_t \le \mathrm{DIM}(v) < b_{t+1} \right\}, \quad (5)$$

$$b_t = \frac{\max\{\mathrm{DIM}\}}{N} t, \quad t = 0, 1, 2, \ldots, N-1. \quad (6)$$

Here, max{DIM} is the maximal value of the DIM over the entire set of short-scan view angles, which can be denoted by Θ, where Θ is the set of all view angles. Consistency classes satisfy the following non-overlapping conditions: $C_i \cap C_j = \varnothing, \forall_i \ne j$; and $\cup_{t = 0, 1, \ldots} C_t = \Theta$. The number of consistency classes N, needs to be optimized based on different imaging applications. Since there are no common view angles among different classes, the data sorting scheme is uniquely determined by the number of consistency classes, N. After data sorting, data within each consistency class have similar levels of consistency with the corresponding projections of the prior image, and data within different consistency classes represent different levels of data inconsistency corresponding to consistent projections generated from the prior image.

B. Brief review of the SMART-RECON method

Using the defined DIM and gDIM concepts, the acquired projection data set can be sorted into N different consistency classes. However, the challenge now becomes how to reconstruct images for each consistency class since the data sufficiency condition for each consistency class is violated. In this paper, we will show that a previously published iterative image reconstruction method by the author's group, which has been referred to as synchronized multiartifact reduction with tomographic reconstruction (SMART-RECON) [29], can be used to simultaneously reconstruct images for all consistency classes.

1) Construction of the spatial-spectral image matrix: According to the DIM-based data sorting scheme, the data set is retrospectively sorted into N consistency classes. Each class then corresponds to a column image vector containing M voxels and the total of N image vectors can then be arranged into a spatial-spectral image matrix X. Each column of X represents an image vector in the corresponding consistency class and each row of X represents the image value of a given voxel in different consistency classes.

2) Formulation of the SMART-RECON method: The SMART-RECON algorithm was formulated to solve the following convex optimization problem:

$$\widetilde{\mathbf{X}} = \underset{\mathbf{X}}{\operatorname{argmin}} \left[\frac{1}{2}(\overrightarrow{\mathscr{Y}} - \mathscr{A}\overrightarrow{\mathbf{X}})^{\mathrm{T}} \mathrm{D}(\overrightarrow{\mathscr{Y}} - \mathscr{A}\overrightarrow{\mathbf{X}}) + \lambda \|\mathrm{X}_A\|_*\right], \quad (7)$$

where $\overrightarrow{\mathscr{Y}}$ is the vectorized projection data concatenated one consistency class after another, and $\overrightarrow{\mathrm{X}}$ is the vectorized spatial-spectral image matrix X. The diagonal matrix D has the raw counts of the measured data before the log-transform as its diagonal elements. $(\cdot)^{\mathrm{T}}$ denotes the matrix transpose operation. The parameter λ is introduced to control the balance between the data fidelity term and the regularizer strength. The prior image vector, $\overrightarrow{X^p}$, can be used to augment X to generate an augmented spatial-spectral matrix X_A as follows:

$$\mathbf{X}_A = (\overrightarrow{X}^p \mid \mathbf{X}) := \begin{pmatrix} X_1^p & X_1^1 & X_1^2 & \cdots & X_1^N \\ X_2^p & X_2^1 & X_2^2 & \cdots & X_2^N \\ \vdots & \vdots & \vdots & \ddots & \vdots \\ X_M^p & X_M^1 & X_M^2 & \cdots & X_M^N, \end{pmatrix}, \quad (8)$$

and the nuclear norm of this augmented image matrix was used as the regularizer in the SMART-RECON algorithm as shown in Eq. (7). Namely, the regularizer is given as follows:

$$\|\mathbf{X}_A\|_* = \|\mathbf{U}\Sigma\mathbf{V}^{\mathrm{T}}\|_* = \sum_r \sigma_r, \quad (9)$$

where $\mathbf{X}_A = \mathbf{U}\Sigma\mathbf{V}^{\mathrm{T}}$ is the **SVD** of the matrix $\mathbf{X}_A$. In this decomposition, **U** and **V** are two orthogonal matrices, and $\mathbf{\Sigma} = diag\{\sigma_r\}$ is a diagonal matrix with the singular values of $\mathbf{X}_A$, σ_r (r = 1, 2, …), as the diagonal entries. The pseudo-code and other numerical implementation details of SMART-RECON can be found in the previously published paper [29].

Similar to any other iterative image reconstruction method, it is important to investigate the numerical convergence of the SMART-RECON. A detailed study was conducted and results were presented in [30] (please see the on-line supplementary materials in paper [30]) to address this issue. As shown there, numerical convergence of SMART-RECON can be reached either without a prior image or with a short-scan FBP image as the prior image.

III. Materials

To validate the central hypothesis in this paper—*the empirically defined DIM and gDIM can be used to classify a short-scan CT projection data set into several consistency classes and SMART-RECON can be applied to simultaneously reconstruct the corresponding image in each consistency class to reduce image artifacts caused by data inconsistency*—both numerical simulations with a known ground truth and data acquired from *in vivo* human subjects have been utilized. The experimental design, data acquisition parameters, and performance evaluation metrics are presented in this section.

To validate the proposed data consistency driven image reconstruction framework, it is important to answer the following questions:

- How does one quantify the severity of spectral-inconsistency induced artifacts and limited-view artifacts?
- What is the quantitative correspondence between the severity of artifacts caused by spectral inconsistency presented in the FBP reconstructed image and the level of data inconsistency?
- How to jointly determine the optimal number of consistency class N and regularization strength λ to achieve both low spectral-inconsistency induced artifacts and negligible limited-view artifacts?
- How does one demonstrate that the proposed framework can simultaneously mitigate the spectral inconsistency image artifacts and the limited view artifacts in each consistency class provided the data acquisition protocol used automatic exposure control (AEC)?

To answer the above questions, it is important to have a phantom with human anatomy and known ground truth to conduct a performance quantification.

A. Numerical anthropomorphic phantom

To construct the needed digital phantom, a clinical cone beam CT image volume of a human head was used (an example axial slice is shown in Fig.1 (a) and a coronal slice is shown in Fig.1 (b)). The clinical image volume was segmented into three components: air, bone and soft tissue. The tissue attenuation coefficient values for bone and soft tissue are set according to the linear attenuation coefficients of these two tissue types provided by the NIST website as shown in Fig.1 (c). This anthropomorphic digital phantom provided both realistic human anatomy and known truth required for quantitative evaluation.

B. Data acquisition parameters used in numerical simulations

To simulate the variation of tube potential in a data acquisition with AEC, the change of tube potential with view angle is shown in Fig.2 (a). Twenty polychromatic x-ray spectra, from 70 kVp to 90 kVp with a 1 kVp increment, were generated by the Spektr software package [33]) with added filtration of 0.1 mm Cu. Five of these spectra are shown in Fig.1 (d) as examples. Line integrals of the anthropomorphic phantom were generated via a ray-driven implementation of forward projection. The detected photon counts were calculated via the polychromatic Beer-Lambert law with entrance photon fluence of $I_0 = 10^6$ photons/ray. Poisson noise was added to the detected photon counts on a ray-by-ray basis.

C. Data acquisition geometry used in numerical simulations

The imaging data acquisition geometry used in numerical simulations mimics a C-arm cone beam CT acquisition platform (Artis zee, Siemens AX, Forcheim, Germany) used in the data acquisition for human subjects described later. An image matrix size of 256 × 256 × 256, corresponding to a 0.78 mm× 0.78 mm× 0.78 mm voxel size, was used in image reconstruction. 248 view angles were acquired over the 200° short-scan angular span with 20° cone angle and 616 × 480 detector elements across the entire scanning field of view.

Using the numerical anthropomorphic phantom, the quantitative correspondence between the severity of artifacts in the FBP reconstructed image and the level of data inconsistency was investigated. The trade-off between the severity of spectral-inconsistency artifacts and limited-view artifacts was explored to optimize the number of consistency classes and the regularization strength jointly. The mean intensity value, image noise, and reconstruction accuracy were quantified for different reconstruction methods (short-scan FBP, limited-view PICCS [13], and limited-view SMART-RECON). Finally, the convergence behavior was demonstrated quantitatively.

D. Hybrid phantom to study metal artifact reduction using the proposed data consistency driven image reconstruction framework

When a metal implant is present in an image object, the spectral inconsistency artifacts are exacerbated and so-called metal artifacts appear. It would be important to see whether the proposed image reconstruction framework can help reduce metal artifacts. To do so, another numerical phantom was constructed. In this phantom, as in the previous one, an image volume of a non-contrast enhanced cerebral cone beam CT scan was used as the anatomical background. Dental fillings made from copper were inserted in the space between the teeth. The energy dependent linear attenuation coefficient of copper follows the measurement in NIST. The simulated x-ray spectrum was the same as the 80 kVp spectrum shown in Fig.1 (d). Different numbers of dental fillings were distributed in different image slices so that the dependence on the distribution of metallic objects could be investigated.

Using this hybrid phantom, the following two important questions were studied:

- Could the proposed method improve image quality when metallic objects are present?
- How does the distribution of metallic objects impact the performance of the proposed framework?

E. Human subject studies

In addition to numerical simulations, *in vivo* human subject data were used to evaluate whether the proposed framework enables the reconstruction of complex anatomy using a clinical C-arm CBCT system with tube potential modulated by the AEC.

Human subject data sets were acquired using a C-arm image acquisition platform (Artis zee, Siemens AX, Forcheim, Germany). The angular span of the data acquisition was a short-scan angular span with a 20° cone angle (total scan range is 200°). The total data acquisition time was 6 seconds per acquisition, and a total of 248 cone beam projections were acquired over the 200° angular span. Each cone beam projection includes 616 × 480 measured line integrals. An image matrix size of 256×256×256 was used to reconstruct the entire image volume for each time frame. The reconstructed volume had isotropic spatial resolution of

0.78 mm× 0.78 mm× 0.78 mm voxel size. The goal is to demonstrate the clinical feasibility of the proposed method with reduced beam hardening artifacts which are difficult to correct for due to the use of AEC which changes both tube potential and tube current during data acquisition.

F. Evaluation Metrics

To better quantify the attenuation coefficients of the image corresponding to each individual consistency class, the group of reference images were defined as follows. First, four different projection datasets were generated individually using a single polychromatic spectra with a fixed tube potential for each consistency class. Each dataset was generated using the short-scan angular range and the fixed tube potential. Then, the standard FBP with Ram-Lak filter was used to reconstruct the reference images of each of these datasets. These images were used as a reference to quantitatively assess reconstructed images of spectral-averaged FBP, spectral-resolved PICCS, or spectral-resolved SMART-RECON using projection data acquired with varying tube potentials (shown in Fig.2 (a)) at each consistency class. Although spectral-inconsistency artifacts may present themselves in each of these images due to the use of a polychromatic spectrum, these reference images are free of limited-view artifacts and free of spectrum variation-induced artifacts that the proposed method aimed to address. For comparison, the same water attenuation coefficients were used to convert image values into Hounsfield units for all images.

1) Quantification of Spectral Inconsistency Artifacts (SIA) and Limited View Artifacts (LVA): To assess artifacts that may potentially be associated with the proposed reconstruction method, two metrics were introduced to quantify the level of spectral-inconsistency artifacts and the level of limited-view artifacts. Note that the limited-view artifacts are primarily associated with a deformation of high contrast objects such as bony structures, while the spectral-inconsistency artifacts primarily impact the reconstruction accuracy of soft tissues in an image. Therefore, we will isolate bony structures from soft tissues using their corresponding masks generated as follows.

Let X_{ref} be the reference image. To isolate highly attenuating objects from soft tissue, an intensity-based segmentation was performed over X_{ref} to generate a bone mask M_{bone} and a soft tissue mask M_{soft}. For a given class t, the difference between the reconstructed image, X^t, and the corresponding reference image, X^t_{ref}, is an error image that contains spectral-inconsistency image artifacts, limited-view artifacts and noise. An entry-wise Hadamard product of the generated bone mask M_{bone} and this error image was used to isolate the limited-view artifacts. Likewise, the soft tissue mask M_{soft} was used to isolate the soft tissue content in the difference image. The total normalized squared error was then calculated to quantify the corresponding artifacts level as follows:

$$\text{SIA:} = \frac{\sum_t \left\| M_{\text{soft}} \circ (X^t - X^t_{\text{ref}}) \right\|_2}{\sum_t \left\| M_{\text{soft}} \circ X^t_{\text{ref}} \right\|_2}, \quad (10)$$

$$\text{LVA:} = \frac{\sum_t \left\| M_{\text{bone}} \circ (X^t - X^t_{\text{ref}}) \right\|_2}{\sum_t \left\| M_{\text{bone}} \circ X^t_{\text{ref}} \right\|_2}, \quad (11)$$

where ○ is the Hadamard product, SIA denotes the level of the spectral-inconsistency artifacts, and LVA denotes the limited-view artifacts in the reconstructed image series. To evaluate the total artifacts level (TAL), the above metrics are combined into a new metric defined as follows:

$$\text{TAL} = \log_{10}(\sqrt{(\text{SIA})^2 + (\text{LVA})^2}). \quad (12)$$

The TAL was used to optimize the reconstruction parameters: the number of consistency classes N and the regularization parameter λ.

2) Quantification of overall reconstruction accuracy: The overall reconstruction accuracy was quantified by the relative root mean square error (rRMSE),

$$\text{rRMSE}(t) = \frac{\left\| X^t - X^t_{\text{ref}} \right\|_2}{\left\| X^t_{\text{ref}} \right\|_2} \times 100\%, \quad (13)$$

The rRMSE reflects spatial and spectral inaccuracies in the reconstruction as well as the image noise level.

IV. Results

A. Results of numerical anthropomorphic phantom studies

1) Investigation of the relation between the level of data inconsistency and the severity of image artifacts: Based on the definition of the DIM, the relationship between the level of data inconsistency and the severity of image artifacts was investigated and results are shown in Fig. 3. In this section, there is only one view angle classification, corresponding to FBP reconstruction over the entire short scan angular range. Therefore, gDIM and SIA are evaluated for this single class containing all views. Additionally, LVA is neglected since it is not applicable here.

When the monochromatic x-ray spectrum (43 keV) was used to generate the projection data, no spectral-inconsistency artifacts can be observed in the FBP reconstructed image. As expected, there is no variation of the DIM over view angles.

When the polychromatic spectrum (70 kVp tube potential with a mean energy of 43 keV) was used, the results depend upon how wide the spectrum is. When the energy window was limited to a relatively narrow width, such as 43 ± 5 keV, negligible image artifacts and minimal variation of the DIM can be observed. In contrast, when the energy window width was increased to 43 ± 10 keV, minor DIM variations can be observed and the gDIM was increased by a factor of 3 relative to the narrow energy window case. Finally, when the full polychromatic spectrum was used, more severe image artifacts present themselves in the FBP image and a significantly increased gDIM is also observed.

When AEC was simulated by using only two polychromatic x-ray spectra (70 kVp and 90 kVp), as shown in Fig. 3, both the variation of the DIM value and the value of gDIM increased dramatically. In this simulation with two spectra, the first 100° data were generated using a 70 kVp spectrum while the last 100° data were generated using a 90 kVp spectrum. From the generated DIM curve, an observed transition point at 100° can also be observed. Additionally, data are relatively self-consistent within the first 100° view angle range and within the last 100° view angle range. Overall, the high data inconsistency level within the entire short-scan range induces strong spectral-inconsistency image artifacts as shown in visual appearance of image artifacts and quantitative assessment of artifacts level.

Finally, the full AEC was simulated with a quasi-continuous tube potential variation over the view angle range as shown in Fig. 2 (a). Interestingly, the derived DIM curve resembles the variation of tube potential. The similarity between the simulated tube potential variation and the derived DIM curve indicates that the proposed DIM can be used as a good metric to quantify the spectral consistency encoded in data at different view angles.

The level of spectral-inconsistency artifacts was quantified by SIA defined in Eq. (10) and these SIA values were reported in Fig. 3 as well.

2) Optimization of reconstruction parameter: To quantify the change of the TAL values with the number of consistency classes N and the regularization strength λ, the TAL values were calculated from the reconstructed images volumes on a grid of parameter (N, λ). For convenience, the regularization strength λ is expressed as a percentage of the maximal singular value σ_1 produced by the SVD of *the initial augmented spatial-spectral image matrix (i.e., in the first iteration).*

Results are presented in Fig. 4. As shown in Fig. 4, the pair of parameters ($N = 4$, $\lambda = 10\%$ of σ_1) yield the lowest overall artifacts level and thus this pair of parameters was selected to be the optimal parameter for reconstruction results presented in the remainder of the paper.

3) Overall image quality assessment: Using the optimized parameters $N = 4$ and $\lambda = 10\%$ of σ_1, images were reconstructed from SMART-RECON and the results are shown in Fig. 5. To obtain a qualitative visual comparison of image quality, prior image constrained compressed sensing (PICCS) [13], which uses the prior image same as SMART-RECON, was also used to reconstruct images for each corresponding consistency class.

The reconstruction results from FBP, PICCS, and SMART-RECON are shown in Fig. 5. Shading bands can be observed across the temporal bones in the FBP reconstruction, but both PICCS images and SMART-RECON images were able to mitigate shading band artifacts caused by spectral inconsistency. However, since data within each consistency class only correspond to a 50° angular span, limited-view artifacts present themselves in the

PICCS reconstructed images as either bright or shading bands. In contrast, negligible limited-view artifacts were observed in SMART-RECON images.

Note that attenuation coefficients in the reference image are different from that of any of the SMART-RECON images since the reference image represents the attenuation coefficient at the selected effective energy of 43 keV.

Quantification results from two carefully selected ROIs are summarized in Fig. 6. These two ROIs (as shown in Fig. 5) were carefully selected to avoid any spectral-inconsistency artifacts. For the reference images, the attenuation coefficient of bone or soft tissue decreases with the increase in tube potential of the spectra used to generate data in each consistency class. This is consistent with the expected results since the attenuation coefficients drop with an increase of the photon energy. Using FBP to reconstruct the short-scan dataset, only one spectral-averaged image can be generated; however, using SMART-RECON, four images representing different spectral information can be reconstructed. Since the variation of attenuation coefficients over energy in SMART-RECON closely matches that of the reference images, this observation suggests that the proposed consistency driven image reconstruction method can potentially achieve spectral-resolved imaging when tube potential changes smoothly with view angle in the data generation process. As a comparison, since limited-view artifacts remain in the PICCS images, intensity values of PICCS images measured within these ROIs are biased and they can not correctly represent the variation of attenuation coefficients over energy.

Results of the overall reconstruction accuracy are summarized in Fig. 7. The reconstruction accuracy of SMART-RECON is a factor of three better than that of the spectral-averaged short-scan FBP and is a factor of four better than that of the PICCS reconstruction for the same consistency class. To quantitatively assess reconstruction accuracy, reference images should be defined appropriately for each class. For each class, we simulated a reference dataset with short-scan angular range as if it were acquired from the mean tube potential within that class. The FBP image of the reference dataset can be considered as a reference image since it is free of limited-view artifacts and free of spectrum variation-induced artifacts. Tube potentials of each class were selected as: 70 kVp ($t = 1$), 75 kVp ($t = 2$), 80 kVp ($t = 3$) and 87 kVp ($t = 4$).

B. Results of metal artifacts reduction: hybrid phantom studies

To demonstrate that the proposed reconstruction framework can be used to reconstruct images with metallic implants, two, three, and four different copper objects have been fused into the human anatomy and the reconstruction results are shown in Fig. 8. Note that when metallic implants are present in the image object, three material thresholding segmentation was applied to generate the needed prior image. More specifically, pixels with a CT number below −500 HU were classified as air. Pixels with a CT number from −500 HU to 500 HU were classified as soft tissue. Pixels with CT number between 500 HU to 3000 HU were classified as bone and any pixels with a CT number higher than 3000 HU were classified as metallic implants.

As shown in the first row in Fig. 8, when metallic objects are present, the DIMs demonstrated a strong dependence on the distribution of metallic objects as opposed to the weaker dependence on the polyenergetic x-ray spectrum (Fig.3). This behavior is intuitive since the spectral inconsistency is primarily dominated by how the metallic objects are distributed rather than the variation in the x-ray spectra.

After the DIM was derived, data were retrospectively sorted into $N = 4$ classes with data sorting windows for each class given as [0, 0.1), [0.1, 0.2), [0.2, 0.3), [0.3, 0.4). SMART-RECON images corresponding to the lowest gDIM are shown in the fourth row in Fig. 8. As a qualitative comparison, the normalized metal artifacts reduction (NMAR) [34] was used to generate the prior image for SMART-RECON and also used to benchmark the performance.

As shown in the third row in Fig. 8, most of the metal artifacts can be neatly mitigated and most anatomical details can be persevered in NMAR images. However, as pointed out by the yellow arrows, detailed teeth and bony structures can be better preserved in SMART-RECON images.

C. Results of human subject studies

Based upon the optimized reconstruction parameters, the short-scan projection dataset acquired from human subject exams was sorted into four consistency classes. As a reference, the clinical reconstruction using all of the acquired projection data over the short-scan angular range was performed to generate a single spectrally-averaged image. It was used to benchmark the performance of the proposed image reconstruction framework.

To demonstrate the overall image quality from clinical reconstructions and the proposed reconstruction framework, representative image slices are presented in Fig. 9. As one can observe in the images, there are no limited-view artifacts present in SMART-RECON images, and spectral inconsistency induced beam hardening artifacts were mitigated when they were compared with the clinical spectrally-averaged reconstructions. Note that for the sake of convenience, only one SMART-RECON image corresponding to the consistency class with the lowest gDIM value was shown and compared with clinical reconstruction.

V. Discussion and Conclusion

In this paper, an empirical data inconsistency metric, i.e., DIM, was introduced to evaluate the level of data consistency for a given CT projection data set on a view-by-view basis. The acquired projection data set was then sorted into different consistency classes using the DIM values associated with each view angle. For each consistency class, a gross data inconsistency metric, i.e. gDIM, was defined to assess the overall consistency level of the data within a given consistency class. Finally, the image vector that corresponds to each consistency class is arranged in a spatial-spectral image matrix and the previously published iterative image reconstruction method, i.e., SMART-RECON, was used to jointly reconstruct the unknown spatial-spectral image matrix. Both numerical simulation studies and *in vivo* human subject studies were used to validate the proposed data consistency driven image reconstruction framework. It has been demonstrated that both beam hardening artifacts and metal artifacts induced by spectral in-consistency in cone beam CT acquisitions can be significantly reduced using the proposed empirical data consistency driven image reconstruction framework. In this framework, there are two key concepts: the first one is the data sorting scheme using the introduced empirical DIM metric, and the second one is the joint, rather than sequential, reconstruction of image vectors from all consistency classes.

The first concept is somewhat straightforward. As long as a metric can be defined to evaluate the data consistency locally for a view angle, then data can be classified into consistency classes. The contribution of this work was to introduce a practical method to evaluate data consistency on a local view by view basis, rather than to globally evaluate the overall consistency of an acquired data set as other analytical data consistency conditions are able to do. The less straightforward concept in this framework is why and how the nuclear norm in SMART-RECON can be used to jointly reconstruct images without suffering severe limited view artifacts, as opposed to these artifacts occurring in other linear image reconstruction methods such as FBP or other iterative reconstruction methods that use spatial regularizers?

As shown in Fig. 7, it is interesting to observe that PICCS images have a higher rRMSE value compared to the conventional FBP. This can be understood as follows: The conventional FBP uses projection data over the entire short-scan angular range to reconstruct an image. Hence, the error between the short-scan FBP image and reference image at each class only quantifies the error due to the potential view-to-view data inconsistency. In contrast, both PICCS and SMART-RECON were applied to projection data from a narrower angular range than that of the short-scan. Therefore, the error quantified for PICCS and SMART-RECON includes both the potential limited-view artifacts and the residual data inconsistency-related error. The fact that the error in PICCS reconstruction is higher than that of the FBP reconstruction indicates that the limited-view artifacts are dominant in the PICCS reconstructed image. In contrast, the lowest rRMSE in SMART-RECON images indicates that the SMART-RECON method can effectively mitigate limited-view artifacts and reduce reconstruction errors induced by both data inconsistency and limited-view artifacts.

A. Locality and sensitivity of DIM

As shown in Fig. 2, it is interesting to observe that the derived DIM (Fig. 2 (b)) is highly correlated to the programmed tube potential variation (Fig. 2 (a)) for the numerical anthropomorphic phantom studies. It is also interesting to ask whether the proposed DIM is necessary given that the tube potential variation could be measured and incorporated into the reconstruction framework to quantify data inconsistencies and guide data sorting. Actually, one needs to notice that the modulation of tube potential in AEC is not sufficiently local to account for data inconsistency induced by high contrast objects in the patient as shown in the case with metallic implants (Fig. 8 (a)). When metallic implants appear in an image object, DIM primarily reflects the number of metallic implants and the spatial distribution of these metallic implants. In this scenario, DIM proposed in this paper is sufficiently local and sensitive to quantify data inconsistency induced by high contrast objects, not just the tube potential variation itself.

B. Transferability of optimal parameters from numerical simulations to experimental studies

Due to the lack of ground truth in experimental studies, it is difficult to optimize reconstruction parameters quantitatively. In this work, parameter optimizations and performance investigations were performed quantitatively in numerical simulations with known truth. To make the parameter optimization transferable to the *in vivo* cases, we specifically constructed an anthropomorphic numerical phantom directly from the anatomy of human head by applying the forward projection operation to the head CT image volume. Geometrical parameters in simulations are the same as that used in the clinical cone beam CT system used to acquire experimental datasets for *in vivo* studies. With these efforts, it is reasonable to believe that the optimized parameters from the numerical phantom study can be fairly reliably transferred to experimental studies. However, for different applications or imaging tasks, the parameters should be optimized separately.

C. Why nuclear norm minimization as regularizer?

To gain some intuitive understanding of the meaning of minimizing the nuclear norm of the spatial-spectral matrix in the example discussed in this paper, let's look into the intrinsic low dimensionality and related properties of the spatial-spectral matrix formulated in terms of the data consistency driven image reconstruction framework.

Using the numerical phantom studies that simulate the effect of automatic exposure control (AEC) in a CBCT data acquisition system, it was observed that as the tube potentials of the x-ray spectra changed with view angle continuously (as shown in Fig. 2 (a)), the derived DIM shown in Fig. 2 (b) changed in a similar manner. According to the DIM-based data sorting scheme, projection data are retrospectively sorted into $N = 4$ consistency classes (as labelled in Fig.2 (b)) from lower to higher DIM value. As a demonstration, the four images in the image matrix with four consistency classes reconstructed by SMART-RECON in the first iteration are displayed in the first row. By applying a singular value decomposition (SVD) to the spatial-spectral image matrix (i.e., $X = U\Sigma V^T$ with orthogonal matrices U, V, and diagonal matrix Σ), the four spatial distributions of coefficients (U_1 to U_4) are shown in the second row, and the corresponding spectral basis functions (V_1 to V_4) are shown in the third row. One can observe that the meaningful spectral variations of the image matrix only appear in the first two spectral bases. The U_1 mainly represents the background spectral variation encoded in the original image matrix. The U_2, however, mainly represents relatively high-order spectral variation, which may be responsible for spectral-inconsistency artifacts (as indicated by yellow circles in U_2). Other bases contain primarily noise, other nonidealities, or represent artifacts caused by the limited-view backprojection operation. This analysis indicates that the intrinsic dimensionality of the spatial-spectral matrix is lower than the number of consistency classes. Therefore, a rank-truncated approximation of this spatial-spectral image matrix can maintain the meaningful spatial-spectral content, while the content of noise and artifacts caused by limited-view backprojection can be rejected in the rank minimization process.

D. Evaluating data inconsistency within each view angle

In this work, the data inconsistency level was only assessed on a view by view basis. Conceptually, it is straightforward to generalize this same metric to evaluate data inconsistency level among projection data within each view angle, and correspondingly, the acquired data can be classified into different consistency classes. However, the challenge is in the image reconstruction part: even if one can classify data into consistency classes, one will need a reconstruction method that can incorporate the data consistency information into the image reconstruction process to generate images with reduced inconsistency artifacts. The SMART-RECON method used in this paper is not sufficient to address the reconstruction challenge in this ray-by-ray inconsistency classification case yet.

E. Limitations and future work

There are several limitations in the current work. First, due to the lack of ground truth, the reference image can only be defined empirically to quantify the spectral fidelity over different consistency classes and assess the reconstruction accuracy. Hence, the rRMSE may underestimate the accuracy of reconstruction. Second, in this work, we only demonstrated that the spectral inconsistency artifacts can be mitigated by the proposed consistency driven image reconstruction framework. It is not yet clear how accurate the spectral information can be maintained in each consistency class. Ideally, when the spectral information within each consistency class is well maintained, it would be possible to perform material decomposition from these spectral-resolved image classes provided that the spectral separation is large enough. This would be a very interesting future research direction, although it is beyond the scope of the current work. Third, given that the data inconsistency is only evaluated on a view-by-view basis, the presented framework is not able to reduce intra-view data inconsistency artifacts. For example, for a uniform and circular image object, the view to view inconsistency is negligible, but the beam hardening induced cupping artifacts still exist. This is caused by the data inconsistency among the projection data within each view angle for which the current framework cannot yet handle. Fourth, the use of square difference between the acquired projection data and the corresponding projection data of the prior image prevents us from being able to distinguish the two potential contributions to DIM: one is the the noise variance and the other is the bias in measurement. Although these two sources always co-exist in a single acquired projection data set, it remains an interesting future research topic to search for much more sensitive data inconsistency metrics to classify data into different consistency classes. This is also true for the classification of cardiac motion induced data inconsistency. Due to the complexity of cardiac motion, some carefully elaborated DIM metrics might be needed to quantify data inconsistency levels in cardiac CT such that the global cardiac motion and local cardiac motion can be better differentiated. Finally, the performance of the proposed framework in handling metal artifacts will need to be systematically investigated using physical phantoms and experimental data acquisition systems. Similar to the beam hardening case, when the metallic object induced data inconsistency does not depend on the view angles, the current data consistency driven reconstruction framework may not be effective in reducing the metal artifacts. These aspects remain to be investigated in future work.

F. Conclusion

A view-to-view spectral data consistency driven image reconstruction framework has been developed using an empirical data inconsistency metric to classify data into different consistency classes and the data consistency information is combined with the previously published SMART-RECOM image reconstruction method. Numerical simulation studies and *in vivo* human subject data have been used to validate the framework and to demonstrate the use of the framework in reducing beam hardening artifacts and metal artifacts that are caused by view to view data inconsistency.

Acknowledgment

The work was partially supported by an NIH grant U01 021183. The authors wish to thank John Hayes and Dalton Griner for their editorial assistance in the writing of this manuscript.

References

[1]. Clackdoyle R and Defrise M, "Tomographic reconstruction in the 21st century," IEEE Signal Processing Magazine, vol. 27, no. 4, pp. 60–80, 2010.

[2]. Katsevich A, "Theoretically exact filtered backprojection-type inversion algorithm for spiral CT," SIAM Journal on Applied Mathematics, vol. 62, no. 6, pp. 2012–2026, 2002.

[3]. Katsevich A, "A general scheme for constructing inversion algorithms for cone beam CT," International Journal of Mathematics and Mathematical Sciences, vol. 2003, no. 21, pp. 1305–1321, 2003.

[4]. Zou Y and Pan X, "Exact image reconstruction on PI-lines from minimum data in helical cone-beam CT," Physics in Medicine and Biology, vol. 49, no. 6, p. 941, 2004. [PubMed: 15104318]

[5]. Zou Y, Pan X, and Sidky EY, "Image reconstruction in regions-of-interest from truncated projections in a reduced fan-beam scan," Physics in medicine and biology, vol. 50, no. 1, p. 13, 2004.

[6]. Pan X, Zou Y, and Xia D, "Image reconstruction in peripheral and central regions-of-interest and data redundancy," Medical physics, vol. 32, no. 3, pp. 673–684, 2005. [PubMed: 15839339]

[7]. Noo F, Defrise M, Clackdoyle R, and Kudo H, "Image reconstruction from fan-beam projections on less than a short scan," Physics in Medicine and Biology, vol. 47, no. 14, p. 2525, 2002. [PubMed: 12171338]

[8]. Chen G-H, "A new framework of image reconstruction from fan beam projections," Medical physics, vol. 30, no. 6, pp. 1151–1161, 2003. [PubMed: 12852540]

[9]. Noo F, Clackdoyle R, and Pack JD, "A two-step Hilbert transform method for 2D image reconstruction," Physics in Medicine and Biology, vol. 49, no. 17, p. 3903, 2004. [PubMed: 15470913]

[10]. McCollough CH, Chen GH, Kalender W, Leng S, Samei E, Taguchi K, Wang G, Yu L, and Pettigrew RI, "Achieving routine submillisievert CT scanning: report from the summit on management of radiation dose in CT," Radiology, vol. 264, no. 2, pp. 567–580, 2012. [PubMed: 22692035]

[11]. Thibault J, Sauer K, Bouman C, and Hsieh J, "A three-dimensional statistical approach to improved image quality for multislice helical ct," Medical physics, vol. 34, p. 4526, 2007. [PubMed: 18072519]

[12]. Sidky E and Pan X, "Image reconstruction in circular cone-beam computed tomography by constrained, total-variation minimization," Physics in medicine and biology, vol. 53, p. 4777, 2008. [PubMed: 18701771]

[13]. Chen G-H, Tang J, and Leng S, "Prior image constrained compressed sensing (PICCS): a method to accurately reconstruct dynamic CT images from highly undersampled projection data sets," Medical physics, vol. 35, no. 2, pp. 660–663, 2008. [PubMed: 18383687]

[14]. Nett BE, Leng S, Zambelli JN, Reeder SB, Speidel MA, and Chen G-H, “Temporally targeted imaging method applied to ECG-gated computed tomography: Preliminary phantom and in vivo experience,” Academic radiology, vol. 15, no. 1, pp. 93–106, 2008. [PubMed: 18078912]

[15]. Chen G-H, Tang J, and Hsieh J, “Temporal resolution improvement using PICCS in MDCT cardiac imaging,” Medical physics, vol. 36, no. 6, pp. 2130–2135, 2009. [PubMed: 19610302]

[16]. Tuy HK, “An inversion formula for cone-beam reconstruction,” SIAM Journal on Applied Mathematics, vol. 43, no. 3, pp. 546–552, 1983.

[17]. Donoho D, “Compressed sensing,” IEEE Transactions on Information Theory, vol. 52, no. 4, pp. 1289–1306, 2006.

[18]. Candès E, Romberg J, and Tao T, “Robust uncertainty principles: Exact signal reconstruction from highly incomplete frequency information,” IEEE Transactions on information theory, vol. 52, no. 2, p. 489, 2006.

[19]. Helgason S, “Radon-fourier transforms on symmetric spaces and related group representations,” Bull. Amer. Math. Soc, vol. 71, no. 5, pp. 757–763, 9 1965.

[20]. Ludwig D, “The radon transform on euclidean space,” Communications on Pure and Applied Mathematics, vol. 19, no. 1, pp. 49–81, 1966.

[21]. John F, “The ultrahyperbolic differential equation with four independent variables,” Duke Math. J, vol. 4, no. 2, pp. 300–322, 6 1938.

[22]. Patch SK, “Consistency conditions upon 3D CT data and the wave equation,” Physics in medicine and biology, vol. 47, no. 15, p. 2637, 2002. [PubMed: 12200929]

[23]. Levine MS, Sidky EY, and Pan X, “Consistency conditions for cone-beam CT data acquired with a straight-line source trajectory,” Tsinghua Science & Technology, vol. 15, no. 1, pp. 56–61, 2010. [PubMed: 20559455]

[24]. Wei Y, Yu H, and Wang G, “Integral invariants for computed tomography,” IEEE Signal Processing Letters, vol. 13, no. 9, pp. 549–552, 2006.

[25]. Hamaker C, Smith K, Solmon D, and Wagner S, “The divergent beam x-ray transform,” Rocky Mt. J. Math, vol. 10, 1980.

[26]. Chen G-H and Leng S, “A new data consistency condition for fan-beam projection data,” Medical Physics, vol. 32, no. 4, pp. 961–967, 2005. [PubMed: 15895579]

[27]. Clackdoyle R and Desbat L, “Full data consistency conditions for cone-beam projections with sources on a plane,” Physics in Medicine and Biology, vol. 58, no. 23, p. 8437, 2013. [PubMed: 24240245]

[28]. Yu H and Wang G, “Data consistency based rigid motion artifact reduction in fan-beam CT,” Medical Imaging, IEEE Transactions on, vol. 26, no. 2, pp. 249–260, 2 2007.

[29]. Chen G-H and Li Y, “Synchronized multiartifact reduction with to- mographic reconstruction (SMART-RECON): A statistical model based iterative image reconstruction method to eliminate limited-view artifacts and to mitigate the temporal-average artifacts in time-resolved CT,” Medical physics, vol. 42, no. 8, pp. 4698–4707, 2015. [PubMed: 26233197]

[30]. Li Y, Speidel MA, François CJ, and Chen G-H, “Radiation Dose Reduction in CT Myocardial Perfusion Imaging Using SMART-RECON,” IEEE transactions on medical imaging, vol. 36, no. 12, pp. 2557–2568, 2017. [PubMed: 28866488]

[31]. Li Y, Garrett JW, Li K, Wu Y, Johnson K, Schafer S, Strother C, and Chen G-H, “Time-resolved C-arm cone beam CT angiography (TR-CBCTA) imaging from a single short-scan C-arm cone beam CT acquisition with intra-arterial contrast injection,” Physics in Medicine & Biology, vol. 63, no. 7, p. 075001, 2018. [PubMed: 29494345]

[32]. Otsu N, “A threshold selection method from gray-level histograms,” Automatica, vol. 11, no. 285–296, pp. 23–27, 1975.

[33]. Siewerdsen J, Waese A, Moseley D, Richard S, and Jaffray D, “Spektr: A computational tool for x-ray spectral analysis and imaging system optimization,” Medical physics, vol. 31, no. 11, pp. 3057–3067, 2004. [PubMed: 15587659]

[34]. Meyer E, Raupach R, Lell M, Schmidt B, and Kachelrieß M, “Normalized metal artifact reduction (NMAR) in computed tomography,” Medical physics, vol. 37, no. 10, pp. 5482–5493, 2010. [PubMed: 21089784]

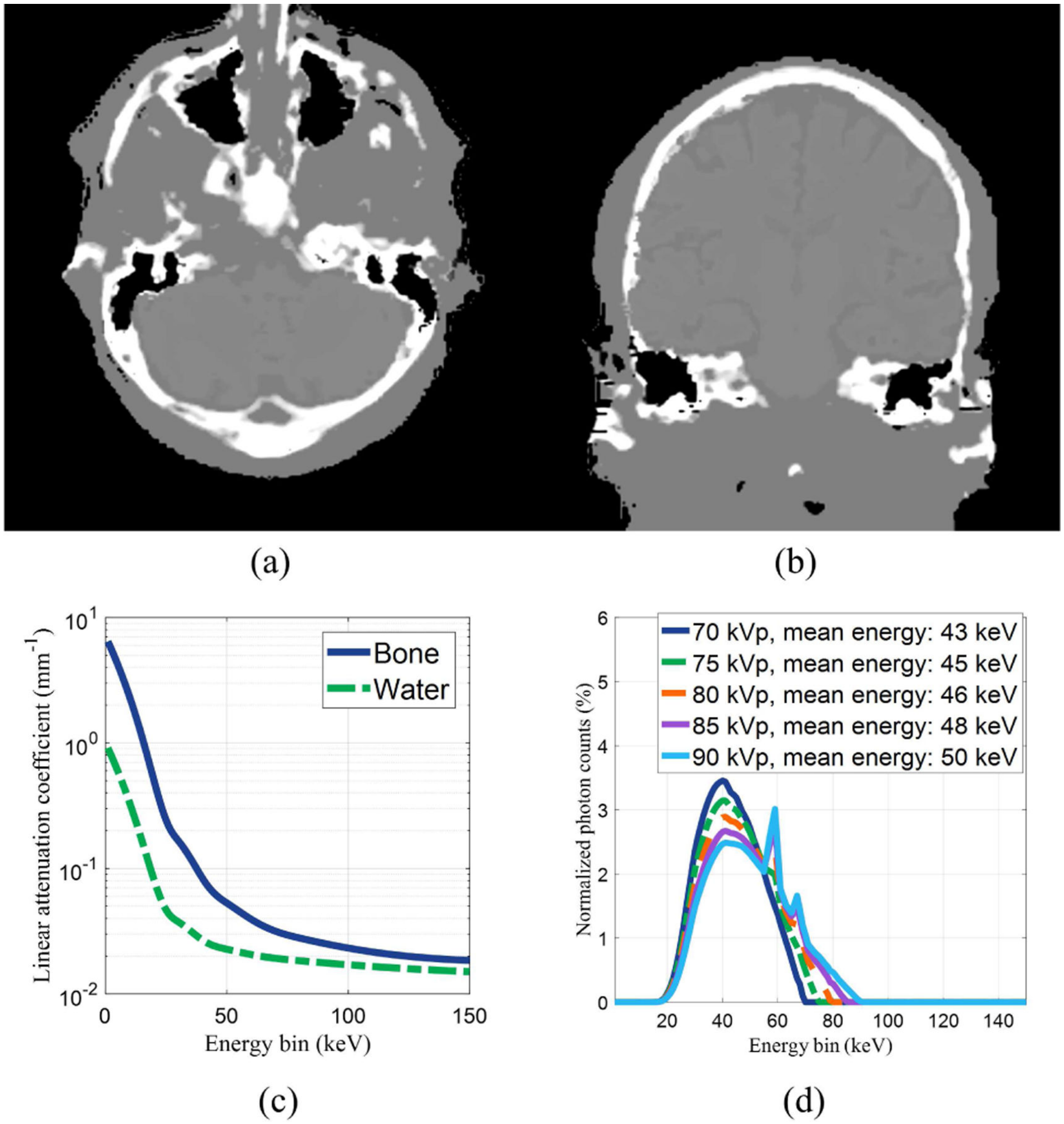

Fig. 1.

Illustration of the anthropomorphic phantom in the numerical simulation studies. (a) and (b): representative axial and coronal slices of the phantom; (c): the linear attenuation coefficients of bone and water; (d) five representative x-ray polychromatic spectra used in the simulation.

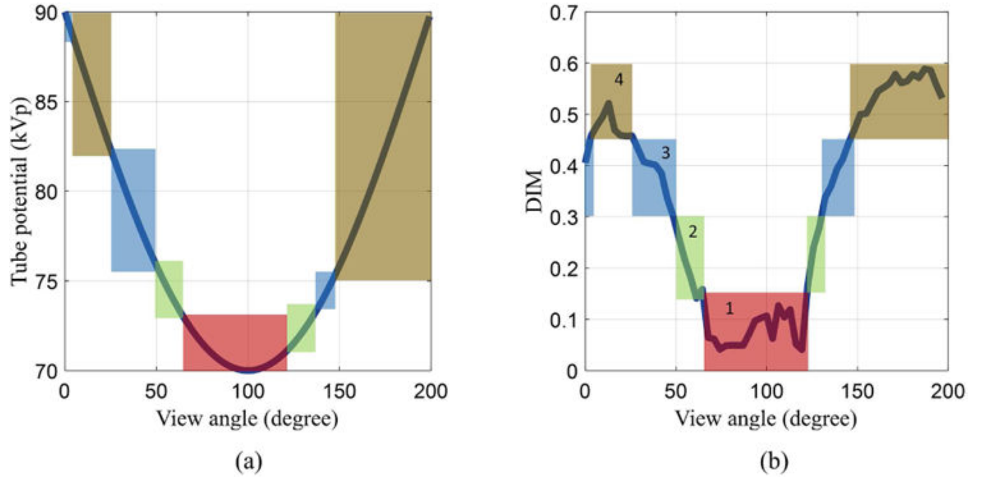

Fig. 2.

Results of numerical anthropomorphic phantom studies. (a) the variation of tube potential over view angle; (b) the derived DIM curve in anthropomorphic phantom studies. Disjointed view angle sets for different consistency classes are labelled by different colors: red for class 1, green for class 2, blue for class 3, and brown for class 4.

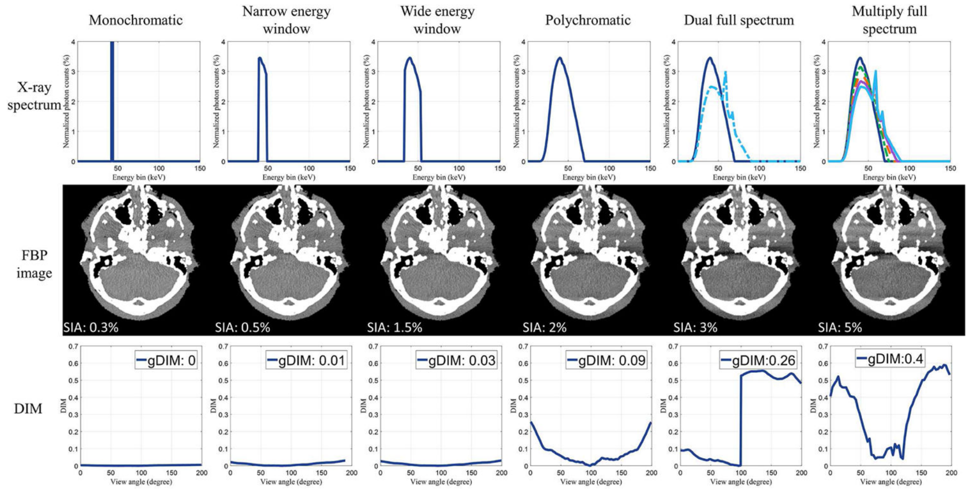

Fig. 3.

Investigation of the correspondence between the level of data inconsistency and the severity of image artifacts.

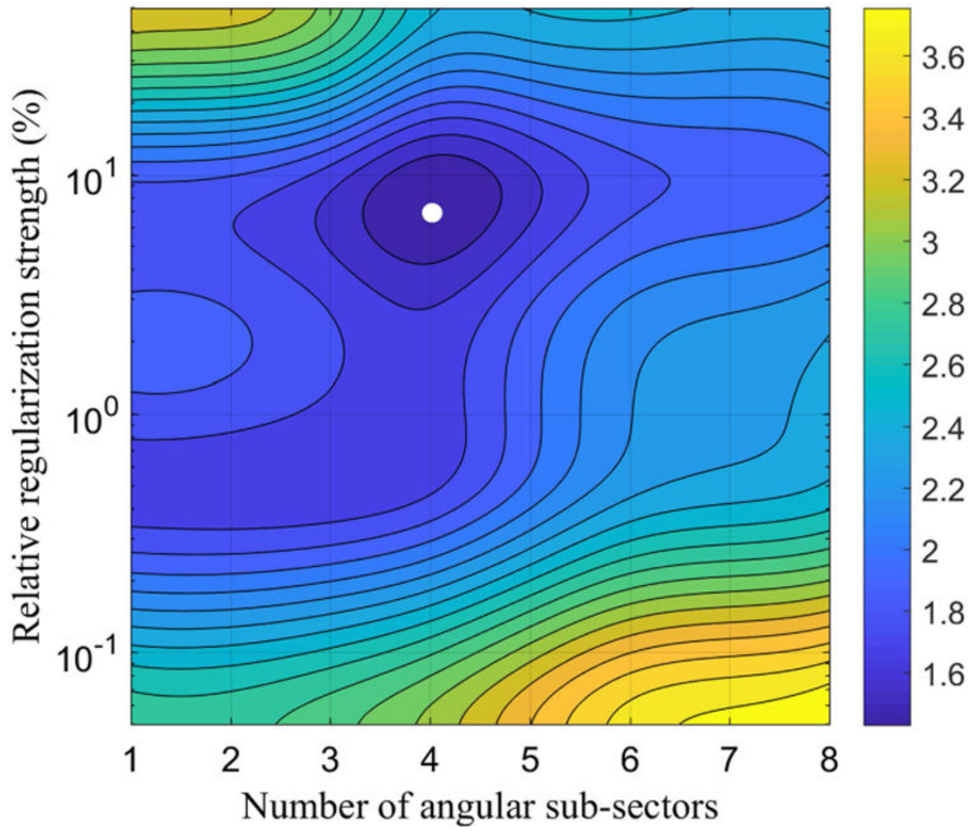

Fig. 4.

Optimization of the number of consistency classes and regularization strength. The lowest artifacts level appear at the point ($N = 4$, λ = 10% of σ_1) as indicated by the white dot in plot. Note that the 2D spline interpolation scheme was used to generate the smooth plot from a discrete grid of data points.

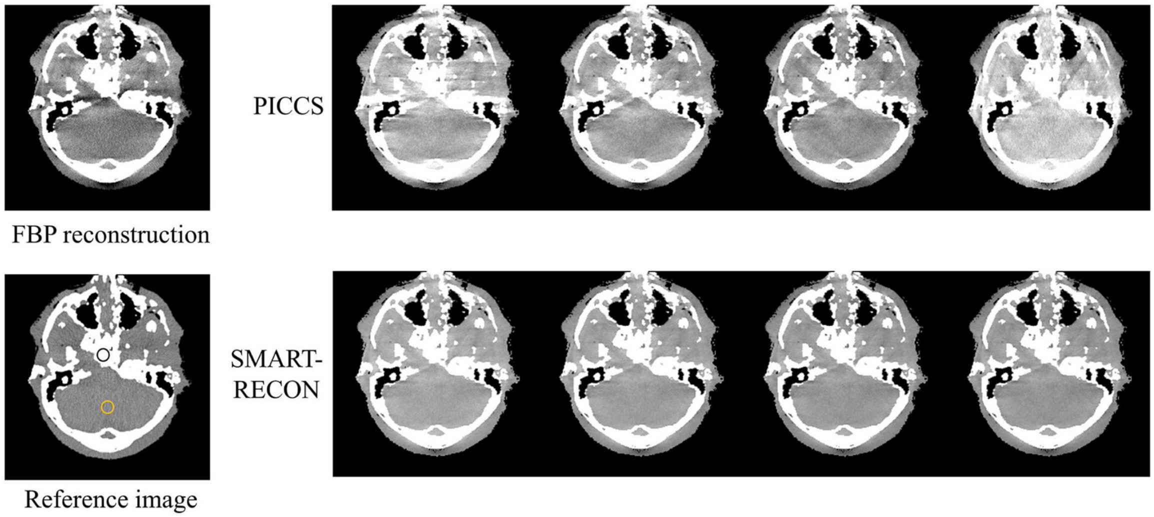

Fig. 5.

Results of anthropomorphic phantom studies using four consistency classes ($N = 4$). For SMART-RECON, the regularization strength of 10% of σ_1 was used. For PICCS, the soft thresholding parameter $\mu = 10$ and prior image parameter $\alpha = 0.5$ were used. The prior image used in PICCS is the same as that used in SMART-RECON. Black circle indicates the ROI selected to quantify intensity value of bone and yellow circle indicates the ROI selected to quantify intensity value of soft-tissue. Images were displayed in W/L: 1000/0 HU.

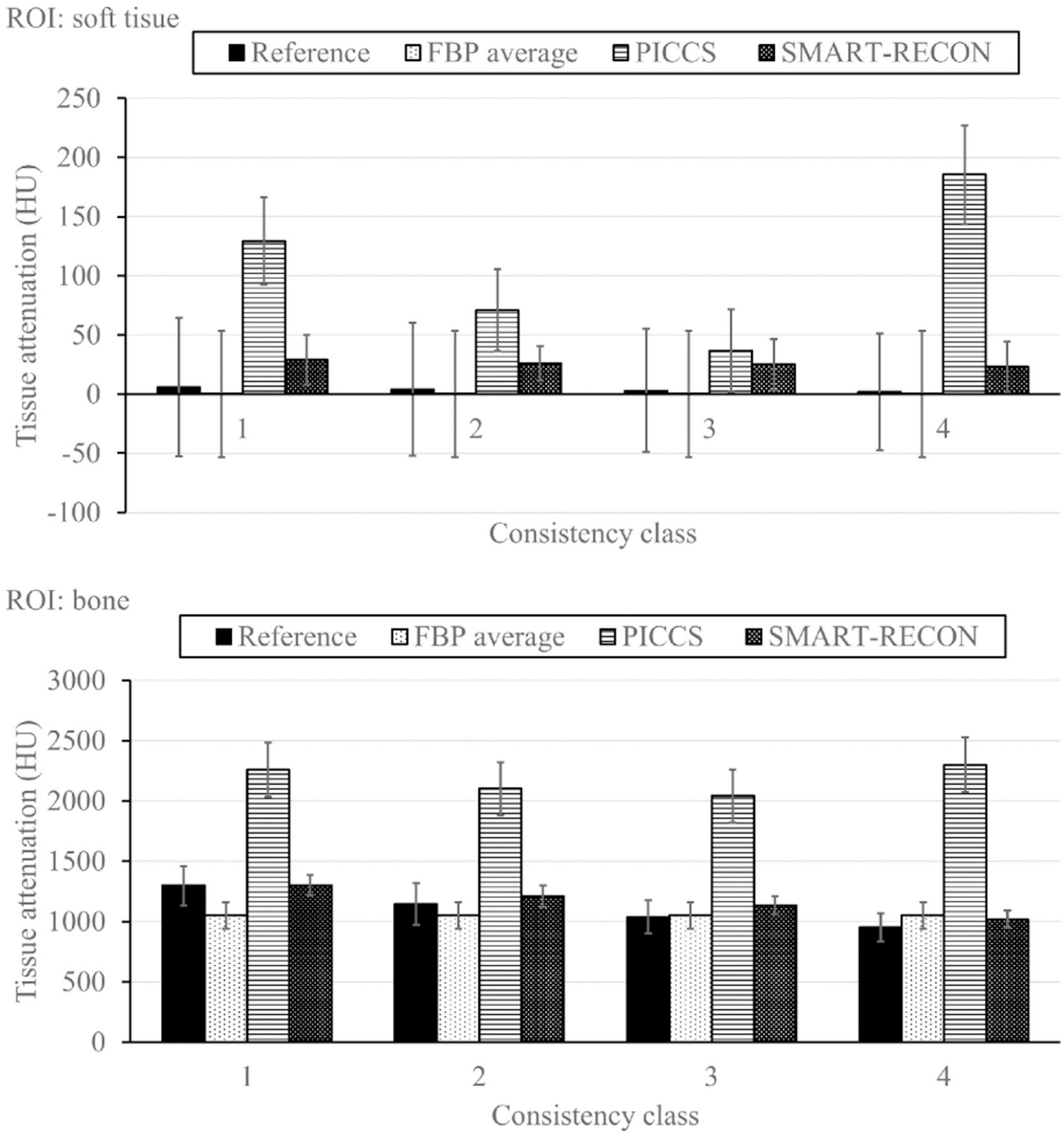

Fig. 6.

The variation of attenuation coefficients over energy of images reconstructed by short-scan FBP, limited-view PICCS and limited-view SMART-RECON. Both PICCS and SMART-RECON images were generated using the same parameters as Fig. 5.

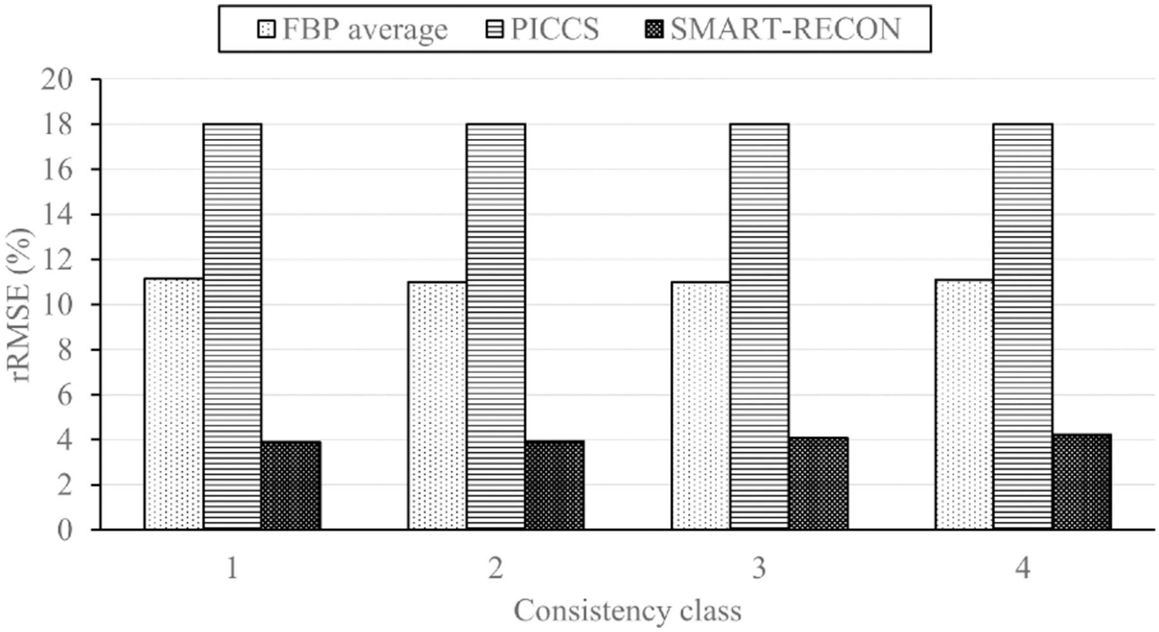

Fig. 7.
The quantification of reconstruction accuracy of the images reconstructed by short-scan FBP, limited-view PICCS and limited-view SMART-RECON. Both PICCS and SMART-RECON images were generated using the same parameters as Fig. 5. ROI selection can be referred to Fig. 5.

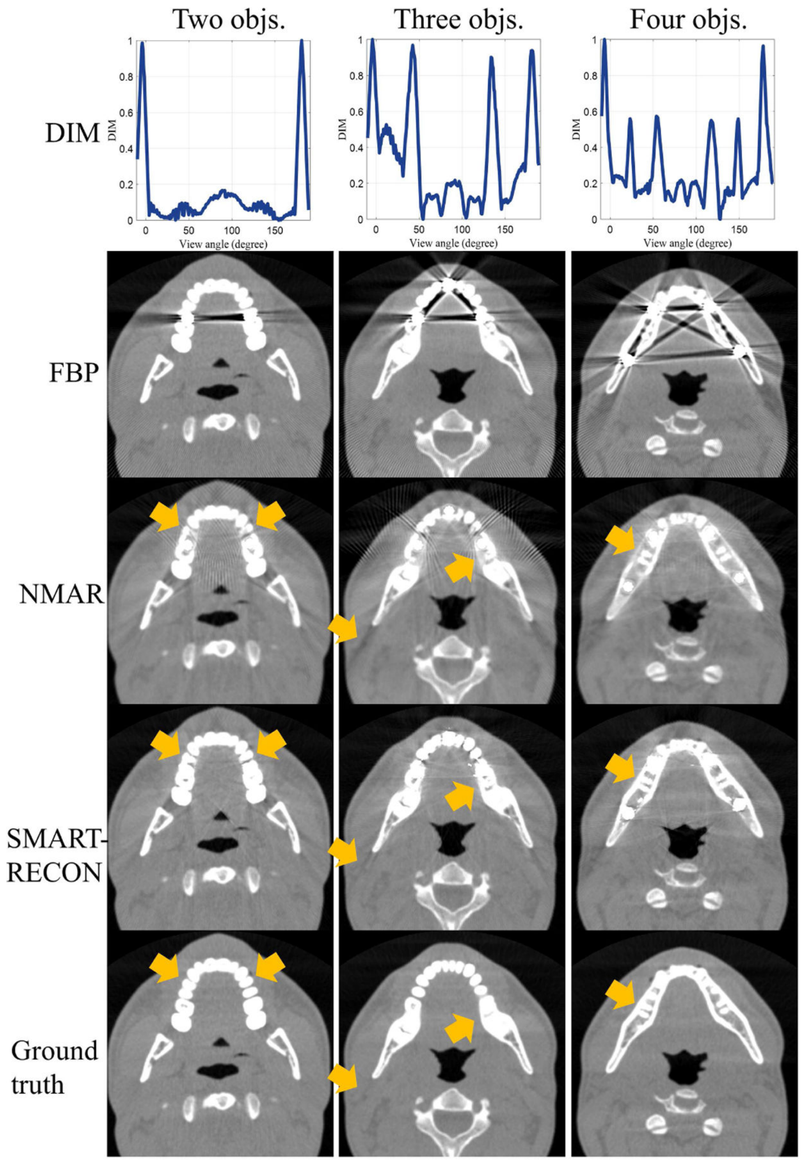

Fig. 8.

Results for hybrid phantom. For SMART-RECON, the regularization strength was optimized as 10% of σ_1. The NMAR images were used to benchmark the performance of the proposed image reconstruction framework. Images are displayed in W/L: 2000/30 HU.

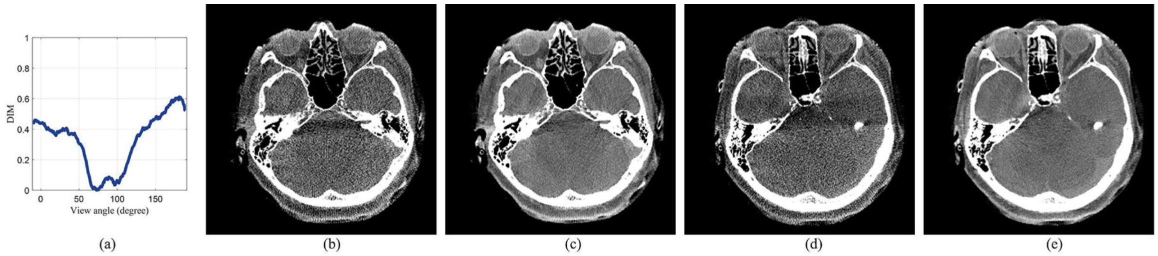

Fig. 9.
Reconstruction results of human subject. (a) the DIM curve; (b) and (d) are clinical reconstruction; (c) and (e) are SMART-RECON images corresponding to the consistency class with the lowest gDIM value. Images were displayed in W/L: 800/150 HU.

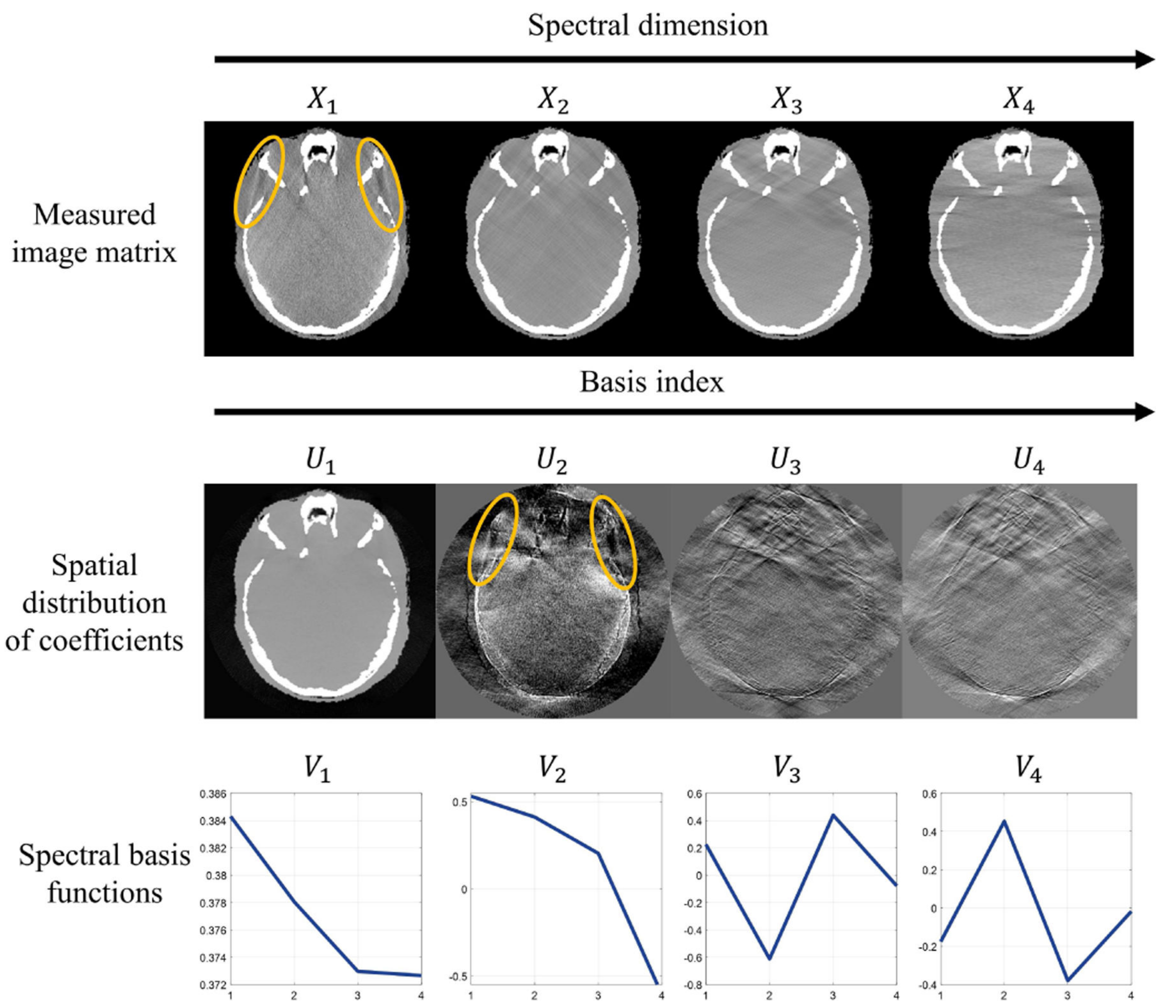

Fig. 10.

Illustration of SVD of a spatial-spectral image matrix. Images in the first row are different columns of the original spatial-spectral image matrix, X. The SVD can be used to decompose the image matrix into three matrices, U, Σ, V^T. Images in the second and third rows are columns of the matrix U and V respectively. Subscript denotes the column index. Images in the first row were displayed with a W/L of 1000/0 HU.